

We are IntechOpen, the world's leading publisher of Open Access books Built by scientists, for scientists

6,900

Open access books available

186,000

International authors and editors

200M

Downloads

Our authors are among the

154

Countries delivered to

TOP 1%

most cited scientists

12.2%

Contributors from top 500 universities



WEB OF SCIENCE™

Selection of our books indexed in the Book Citation Index
in Web of Science™ Core Collection (BKCI)

Interested in publishing with us?
Contact book.department@intechopen.com

Numbers displayed above are based on latest data collected.
For more information visit www.intechopen.com



Characterizing Stress-Strain Behavior of Materials through Nanoindentation

Indrani Sen and S. Sujith Kumar

Abstract

Nanoindentation is a widely used state of the art facility to precisely and conveniently evaluate the mechanical properties of a wide group of materials. Along with the determination of elastic modulus and hardness of materials, this chapter particularly aims to explore the possibilities to assess the corresponding stress–strain characteristics of elastic–plastic materials and most importantly unique pseudoelastic materials. The suitability of continuous stiffness measurement (CSM) based nanoindenter systems along with the adaptability of the instrument without CSM for precisely evaluating the deformation behavior of specialized materials is discussed in details. In this regard, the roll of indenter tip geometry and size is greatly emphasized. The recent research in the field is reviewed thoroughly and the updated protocol generated is illustrated.

Keywords: nanoindentation, stress-strain curve, small-scale, plasticity, NiTi

1. Introduction

Since the early 19th century, indentation technique has been extensively used for characterizing the mechanical properties of vast range of materials. In general, the indentation test is known to measure the *hardness* of materials. In conventional techniques, the mean contact pressure (*MCP*) upon indenting a specimen surface is evaluated. This is done on the basis of the residual area measured from the image of the indent impression and the known value of the applied load. The quantitative parameter, thus evaluated, represents the material's response against deformation. In fact, *MCP* measured at the fully developed plastic zone is known as hardness [1]. With the progress in the technology and its incorporation in the experimental setup, instrumented indentation technique, particularly '*nanoindentation*' has been evolved to assess various mechanical as well as metallurgical properties of a range of materials [2–4]. This includes characterizing elastic moduli, residual stress, creep properties, dislocation density, strain rate sensitivity etc. [5–12]. Among all these developments, the potential of the nanoindentation technique in generating the indentation stress (σ_{ind}) – indentation strain (ϵ_{ind}) curve is the most recent one and it is explained in detail in this present chapter [2, 3].

In nanoindentation, the associated high-resolution depth sensing technique aids to estimate the depth or size of the deformation zone. The process records the continuous response of indentation load (P) in the range of μN vs. indentation

depth (h) in the magnitude of nm . The $P-h$ curve obtained therein helps to assess the various properties of the studied materials. Unlike the conventional technique, in instrumented nanoindentation, hardness is estimated by using indirect measurement of projected contact area from $P-h$ curve and the known geometry of the indenter tip. Similarly, elastic modulus of the material is estimated using the slope of the unloading segment in the $P-h$ response of materials [13]. This method of analysis has been used for various scientific studies to characterize the localized mechanical properties of the samples in sub-micron scale. In fact, this revolutionary modification in the assessment methodology through nanoindentation has opened up a wide range of studies to extract the different relevant mechanical properties of materials on a small-scale.

One of the breakthroughs is the capability of this technique in generating the $\sigma_{ind} - \epsilon_{ind}$ response of a material of interest [3, 14–16]. This novel and recent development plays a significant role in understanding the localized deformation capability of materials system. This is particularly because stress – strain characteristics can provide an insight into the elastic – plastic mechanisms of the materials, as per the conventional notion. In fact, estimation of localized stress – strain characteristics of a material through nanoindentation can even be a substitute for typically used small-scale characterization techniques for instance, micro-pillar compression [17, 18]. Nevertheless, nanoindentation is further beneficial owing to its easier sample preparation, simplicity in experimental execution, and non-destructive nature. This technique therefore has enormous potential for evaluation of small-scale mechanical properties of materials with minimal effort.

Considering this, the present chapter is dedicated to provide a reasonable understanding for generating $\sigma_{ind} - \epsilon_{ind}$ data from the $P-h$ curve of nanoindentation. To develop a more conceptual idea for a new reader, the importance of indenter tip geometry in activating different deformation modes within the indented volume are discussed at the first hand. Subsequently, the basic relationships for the indentation, the method of analysis and generation of protocol for obtaining the $\sigma_{ind} - \epsilon_{ind}$ curve will be discussed.

2. Role of indenter configuration

It is noteworthy that both the uni-axial tensile/compression test as well as the indentation technique are capable to assess the stress–strain characteristics of a material, however, with usually different size-scale of samples along with varying stress-states. The former provides an understanding for the degree of bond stretching induced elastic deformation and dislocation mediated plastic/permanent deformation in the material. To obtain such desired information, the strain-induced into the material should be controlled in such a way that, the material's response reflects the gradual activation and transition from the elastic to the plastic deformation. This is realized in uni-axial deformation without any strain gradient in the specimen, at least macroscopically.

In contrary to that, upon indentation, presence multi-axial state of stress exists beneath the indenter tip. Moreover, the constraint nature of deformation induces strain gradient within the deformation volume. Hence, for assessing the elastic–plastic activity within the deformation zone, the indentation tests need to be specially designed to produce a smooth strain distribution (or gradient) along with its gradual increment. To maintain that, indenter tip geometry needs to be carefully chosen to reflect the $\sigma_{ind} - \epsilon_{ind}$ characteristics from the localized region. In this regard, the most suitable indenter configuration is spherical tip (or sphero-conical indenter).

Before getting into the details about the configuration of the spherical indenter tip and its importance for $\sigma_{ind} - \varepsilon_{ind}$ generation, the reader needs to develop a comprehensive idea about the different type of indenter tips that are used in general. For the same, the geometrical aspect of indenter configuration is briefed here. From a geometrical point of view, indenters are classified into two: (i) geometrically similar indenters (*GSI*) and (ii) non-geometrically similar indenter (*N-GSI*) [4].

The most commonly used sharp pyramidal indenter such as four-sided Vickers (for micro- and macro-indentation) and three-sided Berkovich indenters (for nanoindentation) comes under the category of *GSI*. On the other hand, the spherical indenter falls under the category of *N-GSI*. The major difference in deformation characteristics experienced by a specimen surface, by indenting with any of these two categories of indenter tips can better be appreciated from **Figure 1**. Schematic representations in **Figure 1(a-c)** show the deformation modes activated in traditional elastic-plastic material while increasing the indentation load/depth, using *GSI*. The mathematical relation for geometrical similarity originates from the ratio of the contact radius (a_c) to the maximum depth of indentation (h_{max}). For *GSI*, $a_{c-i}/h_{max-i} = a_{c-j}/h_{max-j} = a_{c-k}/h_{max-k} = \text{constant}$. The subscript, i, j, k signify increasing level of h . Nevertheless, this constant ratio of a_c/h_{max} ensures that the size of the deformation zone of indentation varies uniformly irrespective of the depth of penetration. This helps to estimate the property of the subjected material independent of the applied indentation load/depth. Nevertheless, owing to the sharp nature of the Vickers and Berkovich indenter, the strain-induced within the indentation volume is large enough to generate significant plastic deformation [1]. In that case, dislocation activity is always the dominant mechanism within the deformation volume beneath the indenter tip, irrespective of the change in depth of indentation, as apparent from **Figure 1**. This assists to precisely measure the hardness of a material independent of the indentation load, in the theoretical sense. However, it is realized that *GSI* is not adequate to assess the elastic deformation response of the indented material. In fact, while using conventional Vickers and Berkovich

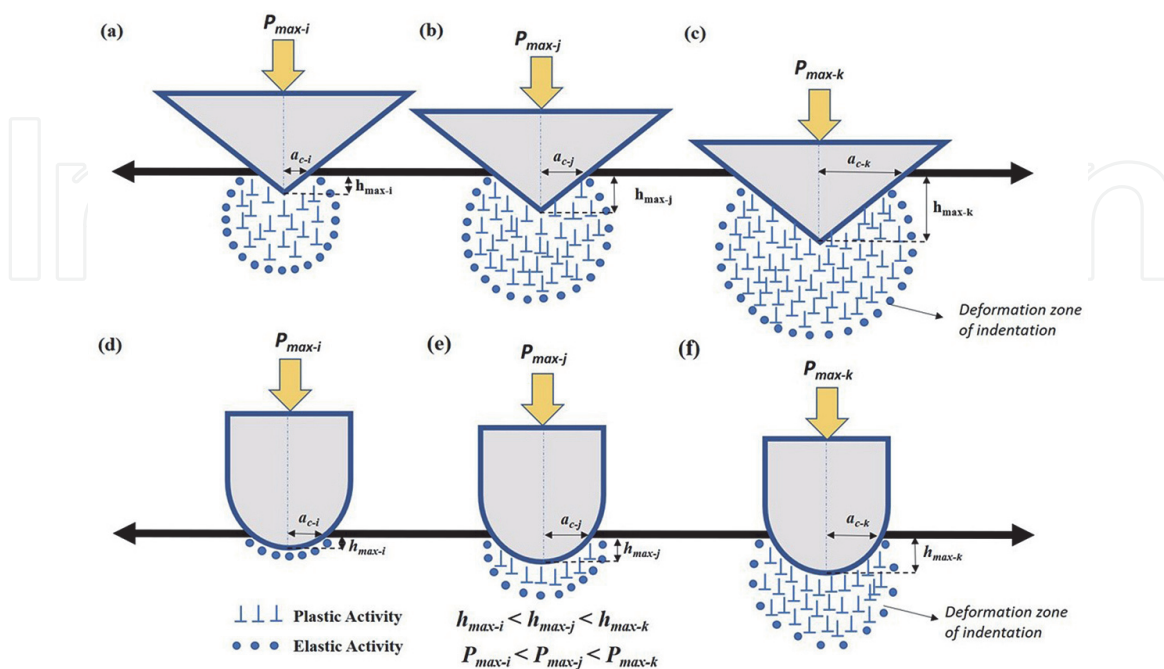


Figure 1. Schematic illustration of the indentation behavior associated with traditional elastic-plastic metallic using (a-c) sharp geometrically similar indenter and (d-e) spherical non-geometrically similar indenter at various indentation depths.

indenters, occurrence of prominent dislocation activity within the deformation volume negates any influence of elastic activity therein. This acts as the limitation of the most commonly using Vickers and Berkovich indenter for generating the stress–strain curve.

On the other hand, a completely different deformation response is being experienced, while the specimen surface is indented using *N-GSI* (spherical tip) with increasing indentation load/depth. **Figure 1(d-f)**, illustrate the deformation scenario within the indentation volume, in such case. It is evident from the figure that, nature of deformation is entirely different in comparison to that for *GSI*. This difference originates from the non-geometrical similarity of the indenter. In case, the specimen surface is indented with a *N-GSI*, $a_{c-i}/h_{max-i} < a_{c-j}/h_{max-j} < a_{c-k}/h_{max-k}$. This essentially means with the progress of the indentation, increment in the contact radius becomes more pronounced with respect to the depth of penetration. Such movement of indenter within the material surface gradually increases the induced strain/stress into the material. Also, the blunt nature of the indenter assists in generating a smooth stress field within the indentation volume, specifically as compared to *GSI*. As a net effect, spherical indenter facilitates a gradual activation of elastic to the plastic deformation mechanism. This potential for gradual instigation of the deformation mechanism similar to that observed in case of uni-axial test, is exploited for $\sigma_{ind} - \epsilon_{ind}$ generation from nanoindentation.

Nevertheless, the most crucial part in this regard is the data analysis procedure that is necessary to convert the indentation *P-h* response into a reliable $\sigma_{ind} - \epsilon_{ind}$ curve. There have been numerous attempts to obtain a stress–strain curve from traditional indentation as well as instrumented one. In the process, the protocol for generation of indentation stress–strain curve has undergone various alterations, to precisely correlate the materials' property. In the next section, we have briefed the different approaches adopted to appreciate the $\sigma_{ind} - \epsilon_{ind}$ behavior of a material. This will help to understand the scientific developments that has been materialized on this particular topic, so far.

3. Evolution of $\sigma_{ind} - \epsilon_{ind}$ generation protocols

The concept for the generation of $\sigma_{ind} - \epsilon_{ind}$ curve from indentation is introduced by Tabor in the 1950s. Tabor has measured the *MCP* on the specimen indented with a spherical tip to estimate the stress that is induced in the process [1]. The most crucial part, however, is the estimation of ϵ_{ind} . Tabor defined ϵ_{ind} by the relation (d/D) , where d is the diameter of the residual impression and D is the diameter of the indenter tip. Here d is measured using the traditional approach, i.e., by imaging of residual impression after unloading. The general trend of $\sigma_{ind} - \epsilon_{ind}$ characteristics of materials, generated following Tabor's protocol, resembles well with that evaluated through traditional uniaxial compression test [1]. However, this method of analysis accounts for only single $\sigma_{ind} - \epsilon_{ind}$ data from an indentation. So, it means that several indentation tests with different indentation parameters are necessary to be pursued, to obtain a continuous $\sigma_{ind} - \epsilon_{ind}$ curve for a material, making the process cumbersome.

Nevertheless, Tabor's approach revealed the potential of the indentation technique and instigated more studies to develop a state-of-the-art protocol for generating $\sigma_{ind} - \epsilon_{ind}$ curve of a material. In this regard, automation through the instrumented indentation has opened up enormous possibilities to generate the $\sigma_{ind} - \epsilon_{ind}$ curve using a single indentation. In turn, the localized deformation behavior of a material can be precisely obtained. First among all is the Field and Swan approach [19]. They have proposed to incorporate multiple partial unload

segments during each indentation. Here, the $P-h$ responses obtained for each particular segments are used to measure the corresponding σ_{ind} and ϵ_{ind} values. The strain, on the other hand, is estimated using the relation a/R_i , where R_i represents the radius of the indenter tip. As per Field and Swan approach, the deformation associated in each unloading segment is assumed to be purely elastic. Correspondingly, the classical Hertzian elastic relationship (explained in the next section by Eq. (1)) is applied on those $P-h$ responses to assess the contact radius, a . From the measured a value, contact area (A_c) is estimated instead of residual impression-based analysis in Tabor's protocol.

The Field and Swan approach has much significance in the present scenario, owing to its implementation of the Hertzian contact mechanics theory. Nevertheless, interpretation of indentation strain as per both Tabor's as well as Field and Swan approaches has been questioned for its integrity with the fundamental concept of strain. In general, strain is defined as the ratio of change in length to the initial length in a region of deformation considered. However, this fundamental relationship is not met in both these above-mentioned approaches.

In order to overcome this fundamental lacking, various studies have been conducted to formulate an adequate relationship for the ϵ_{ind} . Among those attempts, the protocol developed by *Kalidindi* and *Pathak* has succeeded in defining ϵ_{ind} as per the most basic concept of strain [16]. The present chapter is extensively covering the formulation and implementation of *Kalidindi* and *Pathak* protocol for the generation of $\sigma_{ind} - \epsilon_{ind}$ curve for a material subjected to nanoindentation. This protocol is essentially formulated based on classical Hertzian theory, which is explained below.

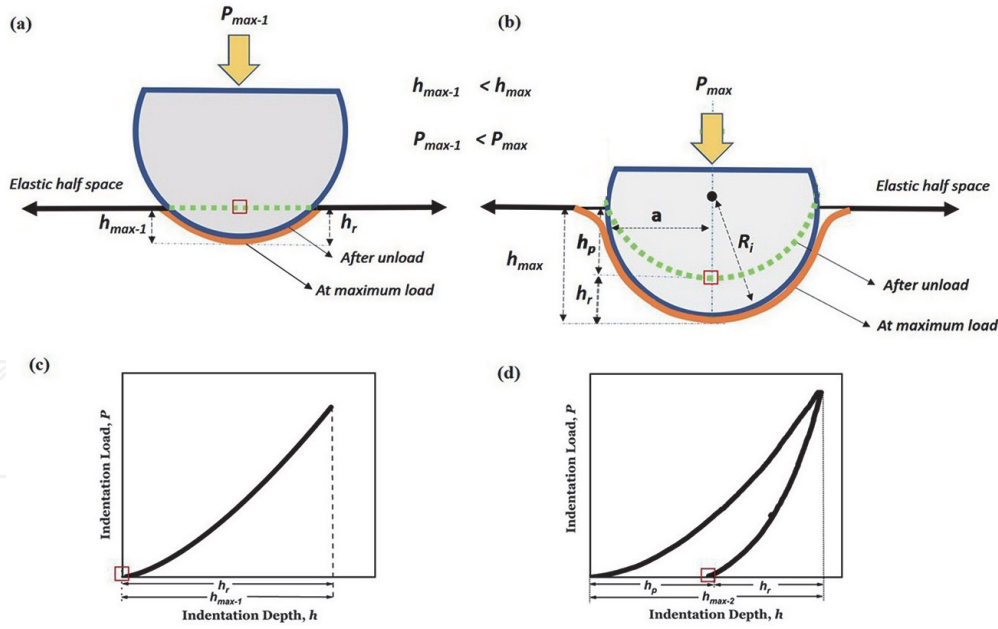
4. Contact mechanics for spherical tip-based indentation

Contact mechanics theory introduced by Hertz has provided a fundamental basis for the indentation technique [20]. Classical Hertzian theory predicts the elastic responses of frictionless contact between two different bodies of dissimilar geometries (with varying properties) in contact. This theory is formulated based on the assumption that material is homogenous and isotropic. In the present scenario of indentation using spherical indenter, the Hertzian theory for elastic contact between the sphere (indenter) and elastic half-space (specimen surface) is used for the formulation of $\sigma_{ind} - \epsilon_{ind}$ generation. In the indentation aspect, the material of interest is considered as an elastic half-space by following the criteria that indenter tip radius (R_i) should be at least ten times smaller than the horizontal dimensions of the sample [21].

As explained in previous Section 2 (see **Figure 1(d-f)**), indentation using spherical indenter tip facilitates the gradual activation of elastic to plastic mechanisms in the material. Therefore, for the sake of understanding, the overall deformation scenario can be categorized into (i) fully elastic and (ii) plastic following the initial elastic section. The schematic representation of these two modes of deformation and their corresponding $P-h$ response is showed in **Figure 2**. In the first case, material recovers all the depth it penetrated upon the indentation (see **Figure 2(a)** and **(c)**). In the second case, some amount of permanent deformation is existing within the indentation volume (see **Figure 2(b)** and **(d)**). Hertz has provided the basis for the elastic deformation associated in two former cases using the relation below,

$$P = \frac{4}{3} E_{eff} R_{eff}^{1/2} h_r^{3/2} \quad (1)$$

$$\frac{1}{E_{eff}} = \frac{1 - \nu_s^2}{E_s} + \frac{1 - \nu_i^2}{E_i}, \quad \frac{1}{R_{eff}} = \frac{1}{R_i} + \frac{1}{R_s} \quad (2)$$


Figure 2.

Schematic representation of indentation of behavior of material in (a) fully elastic condition and in the presence of (b) plastic deformation. Corresponding indentation load vs. indentation depth responses of materials are shown in (c) and (d).

Here P is the applied load, h_r is the recoverable depth, R_{eff} is the effective tip radius and E_{eff} is the effective elastic moduli. All the characteristic terms mentioned here can be appreciated from **Figure 2(b)**. The terms h_{max} and h_p in **Figure 2** represent the maximum depth of indentation at P_{max} and recurring plastic depth of indentation post-unloading (P is zero), respectively. In the Hertzian relation, the role of elastic deformation on the two mating parts is assessed using E_{eff} . The value of E_{eff} accommodates the elastic deformation associated with the hard indenter and soft sample. E_{eff} during the indentation is estimated using the relation (2). Similarly, R_{eff} takes into account the influence of plastic activity on the overall deformation. It is related to the indenter tip radius (R_i) and the radius of curvature of the sample (R_s) upon the indentation. R_{eff} of the sample is estimated using the relation (2).

All these relations derived by Hertz has laid the foundation for the formulation of $\sigma_{ind} - \varepsilon_{ind}$ data from the nanoindentation $P-h$ response. This is explained in details in the following section.

5. Defining the indentation stress and indentation strain

It is well understood from Section 3 that Tabor's and Field and Swan's protocols do not suffice to define the ε_{ind} precisely. Nevertheless, *Kalidindi* and *Pathak* have defined the σ_{ind} and ε_{ind} by considering the size of the deformation zone formed beneath the indenter and correlated it with the fundamental Hertzian relationship [16]. This protocol has succeeded in producing comprehensive $\sigma_{ind} - \varepsilon_{ind}$ data from the nanoindentation experiments (explained in Section 6).

As per this novel approach, eq. (1) is rearranged by incorporating the following relations:

$$\sigma_{ind} = \frac{P}{\pi a^2}; \sigma_{ind} = E_{eff} \varepsilon_{ind}; \varepsilon_{ind} = \frac{4}{3\pi} \frac{h_r}{a} \approx \frac{h_r}{2.4 a} \quad (3)$$

$$a = \sqrt{R_{eff} h_r} \quad (4)$$

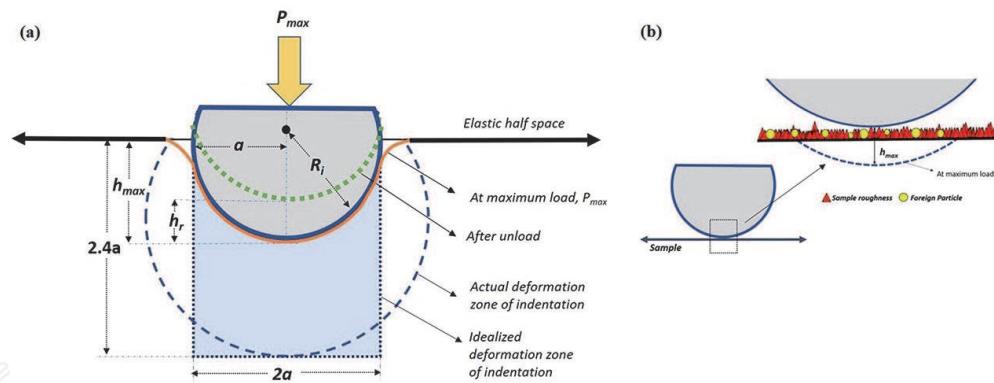


Figure 3. (a) Schematic representation of the deformation behaviour associated with indentation. Figure highlights the actual deformation zone of indentation and the idealized deformation zone of indentation. (b) Schematic representation of surface irregularities on a sample.

The indentation strain defined using the above relationship satisfies the general definition of strain. This can be better appreciated from **Figure 3(a)**. In the figure, the dashed spherical shaped region beneath the indenter tip schematically shows the actual size of the deformation zone upon indentation. Based on the ϵ_{ind} defined from Hertzian relation, the length of the deformation zone beneath the indenter tip at P_{max} is noted to be $\sim 2.4a$. Interestingly, a simulative study on the prediction of indentation behavior strongly agrees with this relation for tungsten and aluminium [16]. This has validated the new definition of ϵ_{ind} , which is derived without any alteration of the fundamental Hertzian relation. This novel protocol is remarkably different yet comprehensive with respect to the other discussed approaches. This is primarily because it basically takes into account the actual size of the deformation zone during the indentation, rather than simply estimating the ϵ_{ind} data using the concept of variation in indent impression.

Furthermore, this novel protocol has provided a reasonable basis for the analogical comparison of indentation behavior using spherical indenter and uniaxial compression test. The overall nature of the material response upon nanoindentation can be considered as the replication of compressing up to a depth of h_{max} on a cylindrical sample of height $2.4a$ and radius a . To visualize it clearly, the idealized deformation zone of indentation and actual deformation of indentation is schematically shown in **Figure 3(a)**. The shape of the actual deformation zone formed is schematically showed as spherical. The reader should be aware that, in reality, owing to the anisotropy in material's properties, the actual shape of the deformation zone of indentation can be slightly different from this schematic representation. It is also noteworthy that with slight alternation in relation (4), h_{max} can be used instead of h_r in the numerator to accommodate the plastic activity [15]. This whole theoretical concept has paved the way for generating $\sigma_{ind} - \epsilon_{ind}$ curve from the $P-h$ signal in nanoindentation. To realize it in a practical scenario, the reader has to understand the necessary steps to follow for obtaining a reliable output.

6. Theoretical conceptualization to experimental execution

As mentioned in Section 1, nanoindentation typically generates a $P-h$ response and its characteristics define the mechanical property of the material indented. Compared to any other characterization technique, particularly, the most commonly used uni-axial tests, the size of the active deformation region for

nanoindentation is extremely small. Therefore, proper measures are necessary at every steps right from the precise sample preparation to the careful data analysis to obtain reliable data.

6.1 Sample preparation

The existence of an artefacts such as scratches or the presence of foreign particles on the surface can influence the $P-h$ signal and thereby the generated $\sigma_{ind} - \epsilon_{ind}$ data. The poorly polished samples create a scratch on the surface, the depth of which can be in hundreds of nanometres. Data recorded from such a region will certainly influence the overall $\sigma_{ind} - \epsilon_{ind}$ characteristics and consequently alter the assessment of the true properties of the material. This can be visualized and understood from the schematic representation in **Figure 3(b)**. In the figure, red coloured triangular shape and yellow coloured circular shape reveal the presence of sample surface roughness and foreign particles respectively. As per the indentation sequence, the indenter will first acquire the data from those artefacts and move to the bulk of the sample. So, actual material which is supposed to show the pure elastic response initially, is now influenced by the presence of sample surface artefacts. As a net effect, the $P-h$ response from the bulk sample is influenced by the surface roughness/foreign particle. Hence, the assessed properties are certainly different from the true ones [1]. In case of conventional uniaxial tests, such misinterpretation of results can be obtained in case a specimen slips upon loading, or even when elastic properties are estimated from a tensile experiment, without attaching an extensometer to the test specimen.

To avoid such issues, well-polished, smooth, flat and plane-parallel specimen should be subjected to nanoindentation. The necessary steps to achieve such artefact free surface vary with the material of interest. However, colloidal silica polish for few hours (minimum 3 h) after the conventional polish using silicon carbide paper with decreasing mesh size and diamond polish is prescribed for metallic specimens, to attain a reasonably good surface condition for the $\sigma_{ind} - \epsilon_{ind}$ generation. Depending on the surface characteristics of the material, electropolishing may also appear to be a better option to minimize the artefacts on the sample surface.

6.2 Conversion of experimental $P-h$ data to effective $P-h$ data

It is noted that theoretical predictions and the experimental outcome may result to some disparities in case of the nanoindentation test. In this regard, it is noteworthy that proper data analysis plays a key role in the generation of $\sigma_{ind} - \epsilon_{ind}$ curve. It is highlighted in the previous section (Section 6.1) that nanoindentation experiments mandate extremely good quality surface finish. Nevertheless, obtaining the required surface finish is difficult in practice. A proper data correction route on the experimentally obtained $P-h$ curve, on the other hand, can negate the role of artefacts on the $\sigma_{ind} - \epsilon_{ind}$ analysis. This step is crucial to compute a reliable stress-strain curve. For the same, effective initial contact point between the indenter tip and the specimen surface is estimated following the “zero-point correction” (*ZPC*). In fact, *ZPC* deals with discarding the data points which are influenced by unavoidable surface irregularities. In turn, the effective contact point is determined on the basis of Hertzian theory which reciprocates the material behavior. According to the type of nanoindentation instrument used, *Kalidindi* and *Pathak* have proposed two different approaches for the data correction using *ZPC*. One is for nanoindenter with (a) Contact Stiffness Mode, *CSM* (or Dynamic Mechanical Analysis, *DMA*) and another for (b) Non-Contact Stiffness Mode, *N-CSM* [22]. These two modes are slightly different in the method of experimentation.

6.2.1 CSM mode or DMA mode

In CSM or DMA mode, harmonic force is imposed in the loading and unloading segment during the indentation. This is highlighted at the inset (a) of **Figure 4**. It can be hypothetically viewed as if the specimen undergoes multiple indentations with minimal depth scale (2 to 4 nm) while conducting a single indentation. Displacement responses corresponding to these harmonic forces are recorded throughout the indentation. These assist in assessing the variation in contact stiffness, S (or $\frac{dP}{dh}$) upon the indentation. Precise determination of S from each steps of CSM leads to estimate the continuous variation in the related properties of materials with increasing h , for example, hardness and elastic modulus changes [22].

In the present scenario, the continuously varying S , h_r , and P are obtained from the CSM mode of the nanoindenter and these signals are used for ZPC. For the same, the Hertzian relation (Eq. (1)) for elastic contact is rearranged into the following relationship,

$$P - \frac{2}{3}h_r S = -\frac{2}{3}h^* S + P^* \quad (5)$$

Here P^* and h^* denote the effective indentation load and depth respectively. A linear regression analysis on relation (5) helps to trace the P^* and h^* values through the slope ($-\frac{2}{3}h^*$) and y-intercept (P^*). Once the P^* and h^* are established, the experimentally generated $P-h$ signal has to be corrected for obtaining an 'effective $P-h$ curve', which is devoid of any influence from the surface artefacts [16].

6.2.2 Non-CSM mode

In N-CSM mode, indentation is performed without harmonic force. This is also highlighted in inset (b) of **Figure 4**. In this particular case, ZPC is performed by recasting the Hertzian equation as per the relation below (derived from Eq. (1)),

$$(h_r - h^*) = k (P - P^*), k = \frac{3}{4} \frac{1}{E_{eff}} \frac{1}{\sqrt{R_{eff}}} \quad (6)$$

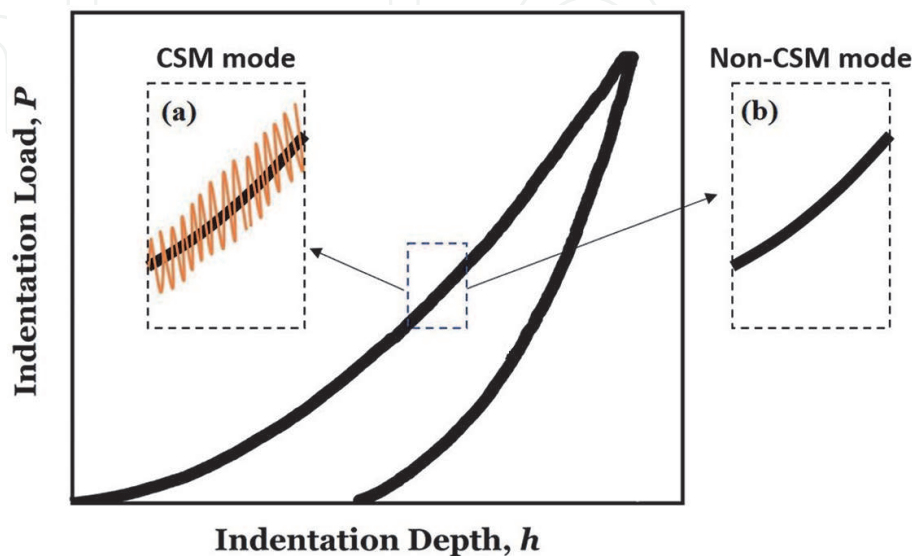


Figure 4. Indentation load vs. indentation depth response generated using nanoindentation. Insets in the figure highlight the method of indentation in CSM mode and N-CSM mode.

In the above relationship, the k value is constant in the elastic segment [15]. It is worth reiterating here that within the elastic segment, continuously varying h equates with h_r , whereas R_{eff} to R_i (explained in the subsequent Section 6.3). Also, prior understanding of elastic moduli of the material makes the calculation much easier. Essentially, regression analysis on the initial elastic segment of experimentally obtained data helps to calculate the values of P^* and h^* and thereby the effective $P-h$ data is estimated.

6.2.3 Selection of data segment

The above-mentioned data correction procedures for nanoindenter with CSM or N-CSM mode, ideally has to be performed on the initial elastic segment of the $P-h$ segment. Such elastic segment dwells within few nanometers, in reality. The exact value of this elastic segment however varies with the sharpness (or bluntness) of the indenter tip and the associated variation in strain gradient [2]. The question here is how to precisely choose a segment in the $P-h$ curve which can be used for the data correction using Eqs. (5) and (6). This can be realized through the iteration process on the initial segment with a different depth limit. For instance, for nanoindentation with h_{max} of 250 nm, regression analysis has to be performed in initial segments with indentation depth of 10 nm (or any other limit) to higher. By doing so, the accurate point of transition from elastic to plastic (data limit) can be approximately finalized based on the continuity nature observed in the effective $P-h$ curve as well as the corresponding $\sigma_{ind} - \epsilon_{ind}$ curve (explained in next Section 6.3).

6.3 Conversion of effective $P-h$ curve to $\sigma_{ind} - \epsilon_{ind}$ curve

As explained in Section 5, the Hertzian relation has provided a basis to obtain $\sigma_{ind} - \epsilon_{ind}$ curve from the $P-h$ response. Once the effective $P-h$ response is computed using the steps mentioned in Section 6.2, Eqs. (3) and (4) are used for obtaining the corresponding $\sigma_{ind} - \epsilon_{ind}$ values. In this conversion process, estimating the continuously varying a is important for calculating the continuous evolution in the σ_{ind} and ϵ_{ind} values. It is particularly evident from Eq. (4) that, a is the main characterizing parameter to obtain the σ_{ind} and ϵ_{ind} values.

Prior to going through further details, the physical significance of a and the mechanisms behind its alteration during indentation are explained through **Figure 5**. The figure schematically shows the indentation behavior of different materials with different extents of elastic-plastic activities. Sample-1 with green color indicates the material with full elastic recovery. Sample-2 (orange) and sample-3 (blue) exhibit the indentation behavior of two materials with different degrees of plastic activities along with elastic deformation. In a fully elastic material (sample-1), the indented surface recovers the whole depth upon the complete removal of load. Thereby R_s attains infinity in this case (see **Figure 5**). So, $R_{eff} = R_i$ for material with full depth recovery (see equation (2)). Similarly, owing to the full recovery, continuously recording h signal can equate with the depth recovery (h_r). In short, $R_{eff} = R_i$ and $h = h_r$ within the elastic regime of material upon indentation.

But, once the dislocation mediated plastic activity is instigated, R_s attains a finite value. The orange and light blue colors in **Figure 5** reveal the formation of finite values of R_s in the materials due to the occurrence of plastic deformation. In these two cases, R_{eff} is no longer equal to R_i . It is reported that R_{eff} is significantly larger than R_i once plastic deformation initiates in the material. Almost a 100-fold increment in the R_{eff} is reported with presence of plastic activity in aluminum sample [3].

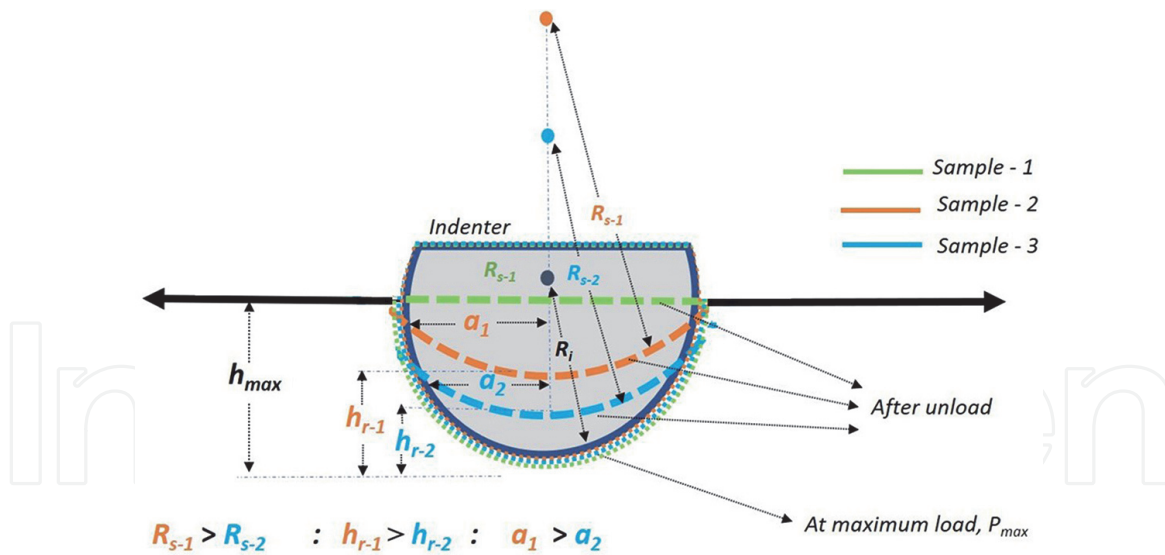


Figure 5. Schematic representation of the nature of deformation volume beneath the indenter tip for materials with three different degrees of elastic-plastic property. Green line shows the sample with full depth recovery. The orange and light blue colors reveal the indentation behaviour of samples with different shares of elastic and plastic activities.

All these physical changes are also related to h_r after the unloading. While comparing sample-2 and sample-3, depth recovery is noted to be higher for the former. Correspondingly, R_s in the material also changes. It is apparent from the **Figure 5** that $R_{s-1} > R_{s-2}$ and $h_{r-1} > h_{r-2}$. As a net effect of change in R_{eff} and h_r , contact between the indenter and sample deflects. This is reciprocated in the changes in a ($a_1 > a_2$). In conclusion, all three parameters are correlated which are primarily controlled by the share of elastic-plastic activities within the material of interest. Eq. (4) derived by Hertz relates all these physical phenomena and in the present scenario, it is utilized to estimate $\sigma_{ind}-\epsilon_{ind}$ curve using relation (3).

6.3.1 $\sigma_{ind}-\epsilon_{ind}$ from CSM nanoindenter

Estimation of a from nanoindentation using CSM mode is straight forward. The interrelation between S and a are derived from Eqs. (1) and (4) according to the Hertzian theory, as shown below:

$$\frac{dP}{dh} = 2 E_{eff} R_{eff}^{1/2} h_e^{1/2} = 2 E_{eff} a \quad (7)$$

$$a = \frac{S}{2 E_{eff}}$$

The analytical significance of this mathematical derivation lies in the fact that unlike Tabor's approach, this expression (eq. (7)) enables to assess the nature of deformation inside the material without a visual inspection of residual impression.

In the data analysis, once the evolving values of a are established using eq. (7), the final $\sigma_{ind} - \epsilon_{ind}$ curve is generated from Eq. (3). **Figure 6(a)** shows $\sigma_{ind} - \epsilon_{ind}$ curves obtained before and after ZPC on experimental $P-h$ data. Interestingly, in this novel protocol, elastic moduli measured from the loading and unloading segments of the $\sigma_{ind} - \epsilon_{ind}$ curve are noted to resemble each other [16]. This observation has validated the new definition for ϵ_{ind} as well as the novel protocol for reliably assessing the mechanical property via $\sigma_{ind} - \epsilon_{ind}$ curve.

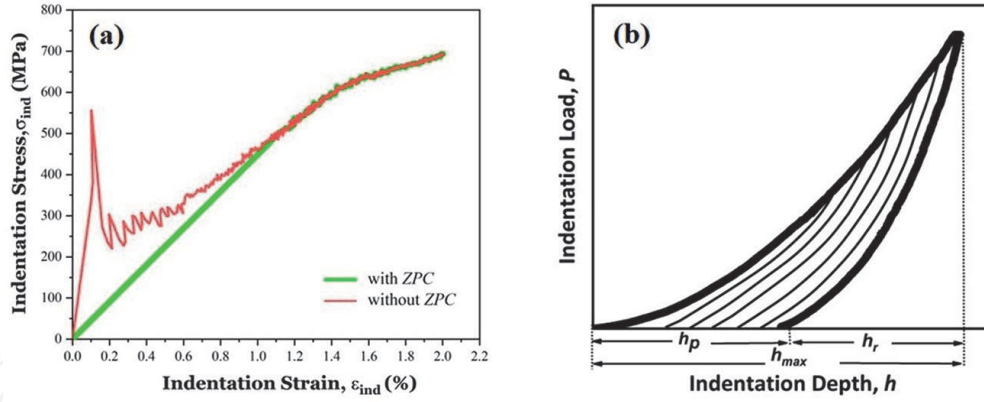


Figure 6. (a) $\sigma_{ind} - \epsilon_{ind}$ curve obtained before and after the zero-point correction. (b) Schematic representation of the $P-h$ responses with multiple unloading segments for generating $\sigma_{ind} - \epsilon_{ind}$ curve in N -CSM measurement nanoindenter.

6.3.2 $\sigma_{ind} - \epsilon_{ind}$ from non-CSM nanoindenter

As compared to the CSM mode, experimentation and method of analysis is different in case of N -CSM mode of nanoindentation. In N -CSM mode, multiple unloading segments are introduced into the indentation test for measuring the evolution in a and thereby the continuous variation in σ_{ind} and ϵ_{ind} values. This is similar to Field and Swan approach in terms of experimentation. **Figure 6(b)** schematically shows the $P-h$ curve obtained after the multiple unloading. Once the effective $P-h$ curve is generated by employing ZPC, following Section 6.2, the evolving values of a are estimated from each segment. For the same, R_{eff} value is estimated by fitting the unloading response using the modified Hertz relation as mentioned below,

$$h_r = h_{max} - h_p = k P^{2/3} \quad (8)$$

here k is a function of R_{eff} and E_{eff} (see relation (6)). E_{eff} can be traced from the prior understanding of elastic moduli of sample or from the initial elastic segment in the $P-h$ curve [15]. So, from the understanding of k value of the respective alloys and the recorded value of h_p with reduction in indentation load in the unloading segments, R_{eff} is estimated by fitting using the relation (8). Once R_{eff} is established, a can be determined from relation (4) and in turn $\sigma_{ind} - \epsilon_{ind}$ curve can be generated using Eq. (3). It is also important to note here that, number of data points in the resultant $\sigma_{ind} - \epsilon_{ind}$ curve depends on the number of unloading segments provided in the experiment.

7. Protocol for $\sigma_{ind} - \epsilon_{ind}$ generation in pseudoelastic shape memory alloys

Previous sections have elaborated the potential of the nanoindentation technique in appreciating the $\sigma_{ind} - \epsilon_{ind}$ characteristics of traditional elastic-plastic metallic systems. In a further extension, *Sujith* and *Sen* have revealed the capability of nanoindentation in assessing the unique pseudoelastic (or superelastic) properties of shape memory alloys (SMA) via $\sigma_{ind} - \epsilon_{ind}$ curve [2, 6]. This recent development has succeeded in the producing the specialized stress - strain characteristics of the pseudoelastic NiTi system using most commonly used N -CSM nanoindenter.

It is noteworthy at this point that as compared to the traditional elastic-plastic metallic alloys, pseudoelastic system is different owing to the occurrence of reversible stress-induced martensitic transformation (SIMT). In pseudoelastic alloys

(some examples of metallic systems are NiTi, Cu-Al-Zn, Cu-Al-Ni, Ni-Ti-Fe, Fe-Mn-Si, Fe-Mn-Si-Co-Ni), parent austenitic phase transforms to product martensitic phase upon the application of stress and it reverts to the previous austenite with the release of stress. Owing to this reversible *SIMT* along with usual elastic deformation in the parent and product phase, the NiTi system in pseudoelastic state shows (8–10) % of recoverable strain. This is also reflected as a unique characteristic in the conventional uni-axial stress - strain curve. Hence, evaluating such unique property using nanoindentation requires special attention in terms of (a) optimizing indentation parameters as well as (b) tailored $\sigma_{ind} - \epsilon_{ind}$ generation protocol. This investigation by *Sujith* and *Sen* is the first of its kind to consider spherical indenter tips with varying R_i as well as P_{max} levels with the aim to identify the optimum combination to precisely evaluate localized pseudoelasticity in *SMA* through nanoindentation. Following steps are briefed:

7.1 Optimizing indentation parameters

For optimizing the indentation parameters, a detailed analysis is performed on the $P-h$ curve obtained from various indenter configuration (R_i of 10 μm , 20 μm and 50 μm) as well as P_{max} (1 mN to 7 mN). Details of the experiments and analysis procedures are reported elsewhere [2]. However, the key observations in this method of analysis are mentioned here.

Optimization of indentation parameters is performed based on the close scrutiny of the experimentally generated $P-h$ curve using Hertzian theoretical prediction and the understanding of the pseudoelastic behavior in the alloy system. **Figure 7(a)** shows the method of analysis performed on the $P-h$ curve. The black solid and the red dashed curves in **Figure 7(a)** show the experimental results and Hertzian theoretical prediction of indentation response, respectively. Using this comparison, overall deformation mode in the indentation is parted into different sections. Correspondingly, the depth of indentation, specifically influenced by pseudoelasticity is assessed. This can be even better appreciated from **Figure 7(b)**. Physical variation associated with indentation volume of NiTi sample using R_i of 10 μm and 20 μm are schematically (in two halves) shown in **Figure 7(b)**. The region influenced by reversible *SIMT* is highlighted as green color in the schematics. This novel method of analysis is performed using a range of combination of indentation parameter. The most adequate combination to assess the pseudoelasticity is identified based on the share of reversible *SIMT* activity and the overall depth recoverability (minimum 90% depth recovery). Based on this systematic analysis, spherical indenter with R_i of 20 μm and P_{max} of 5 mN is noted to be most suitable combination for appreciating pseudoelasticity devoid of the influence of dominant plasticity, in NiTi system.

7.2 $\sigma_{ind} - \epsilon_{ind}$ protocol

Considering the extremely high depth recoverability ($\geq 90\%$) of pseudoelastic NiTi system, following assumption is used while generating the corresponding $\sigma_{ind} - \epsilon_{ind}$ curves,

$$R_{eff} = R_i \text{ and } h_r = h \quad (9)$$

Section 6.3 has already mentioned about the validity of this assumption when material shows full depth recovery. In the present scenario, same assumption is used with depth recovery limit of 90% of the h_{max} . This assists in converting the $P-h$ response into $\sigma_{ind} - \epsilon_{ind}$ curve using Eq. (3), while employing relations (9) in it. Essentially, this new protocol defined the ϵ_{ind} and a using following relation,

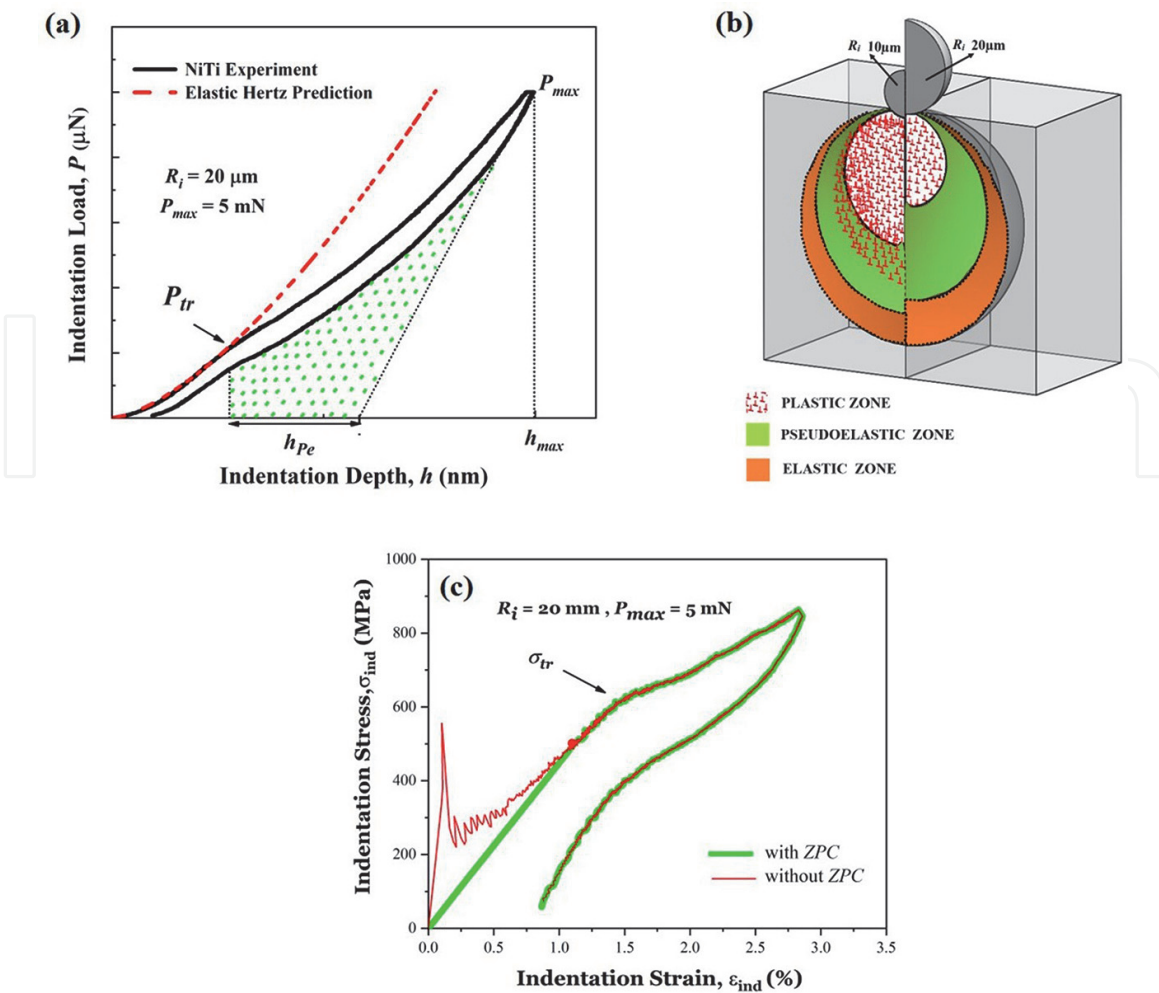


Figure 7.

(a) The P - h response of pseudoelastic NiTi system at its optimized nanoindentation parameter condition ($R_i = 20 \mu\text{m}$ and $P_{max} = 5 \text{ mN}$). Red dotted curve shows the theoretical prediction of P - h response and the green dotted region infers the region that is dominantly influenced by reversible SIMT in the NiTi alloy. P_{tr} in the graph highlights the indentation load at which SIMT initiates in the material. (b) Schematic representation of share of different deformation mechanisms within the nanoindentation volume for pseudoelastic NiTi system indented using R_i of $10 \mu\text{m}$ and $20 \mu\text{m}$. (c) $\sigma_{ind} - \epsilon_{ind}$ curve corresponding to the P - h response (Figure 7(a)). Here, σ_{tr} is the transformation stress to initiate SIMT [2].

$$\epsilon_{ind} \approx \frac{h}{2.4 a} \quad a = \sqrt{R_i h} \quad (10)$$

Prior to conversation of P - h results into $\sigma_{ind} - \epsilon_{ind}$ curve, ZPC is performed following Section 6.2.2. Figure 7(c) shows the $\sigma_{ind} - \epsilon_{ind}$ curve that is generated from the P - h response of NiTi system. Interestingly the curve has shown the signature trends of pseudoelastic system like sudden changes in the transformation strength, plateau strain, significant recovery etc. The transformation strength (σ_{tr}) of the NiTi system estimated from the nanoindentation resembles reasonably well with that derived from uni-axial compression test [2]. This has validated the present protocol for future analysis on smart characteristics of NiTi based shape memory alloys.

8. Closure

The present chapter elucidates the vast potential of nanoindentation technique to develop insights about the localized stress-strain characteristics of materials. Nevertheless, to achieve the $\sigma_{ind} - \epsilon_{ind}$ curve, experiments need to be carefully designed. Also, post indention analysis should be meticulously performed to obtain

the reliable data. Blunt spherical indenter tip is primarily necessary to activate elastic and plastic mechanisms sequentially in the material and thereby to estimate the $\sigma_{ind} - \epsilon_{ind}$ curve. On the other hand, different post-indentation analysis has to be adopted based on the mode of nanoindenter and the material of interest to compute the *indentation stress-strain* data. Validation of the protocols are also discussed for pseudoelastic material systems. The detailed explanation provided in the present chapter based on the physical mechanism associated with different alloy system upon indentation and further data analysis can pave the way for future usage of this method of analysis in various studies.

IntechOpen

Author details

Indrani Sen^{1*} and S. Sujith Kumar^{1,2}

1 Department of Metallurgical and Materials Engineering, Indian Institute of Technology, Kharagpur, India

2 Department of Metallurgical Engineering and Materials Science, Indian Institute of Technology, Bombay, India

*Address all correspondence to: indrani.sen@metal.iitkgp.ac.in

IntechOpen

© 2021 The Author(s). Licensee IntechOpen. This chapter is distributed under the terms of the Creative Commons Attribution License (<http://creativecommons.org/licenses/by/3.0>), which permits unrestricted use, distribution, and reproduction in any medium, provided the original work is properly cited. 

References

- [1] D. Tabor, *The Hardness of Metals*, Oxford University Press, 1951.
- [2] S. Kumar S, I.A. Kumar, L. Marandi, I. Sen, Assessment of small-scale deformation characteristics and stress-strain behavior of NiTi based shape memory alloy using nanoindentation, *Acta Mater.* 16375 (2020) 1–2. <https://doi.org/10.1016/j.actamat.2020.09.080>.
- [3] S. Pathak, S.R. Kalidindi, Spherical nanoindentation stress-strain curves, *Mater. Sci. Eng. R Reports.* 91 (2015) 1–36. <https://doi.org/10.1016/j.mser.2015.02.001>.
- [4] Antony C. *fisher* Cripps, *Nanoindentation*, Springer International Publishing, 2011.
- [5] G.M. Pharr, An improved technique for determining hardness and elastic modulus using load and displacement sensing indentation experiments, *J. Mater. Res.* 7 (1992) 1564–1583. <https://doi.org/10.1557/JMR.1992.1564>.
- [6] S. Kumar S, L. Marandi, V.K. Balla, S. Bysakh, D. Piorunek, G. Eggeler, M. Das, I. Sen, Microstructure – Property correlations for additively manufactured NiTi based shape memory alloys, *Materialia.* 8 (2019) 100456. <https://doi.org/10.1016/j.mtla.2019.100456>.
- [7] J. Hu, W. Zhang, G. Peng, T. Zhang, Y. Zhang, Nanoindentation deformation of refine-grained AZ31 magnesium alloy: Indentation size effect, pop-in effect and creep behavior, *Mater. Sci. Eng. A.* 725 (2018) 522–529. <https://doi.org/10.1016/j.msea.2018.03.104>.
- [8] I.C. Choi, B.G. Yoo, Y.J. Kim, J. Il Jang, Indentation creep revisited, *J. Mater. Res.* 27 (2012) 3–11. <https://doi.org/10.1557/jmr.2011.213>.
- [9] S. Graça, R. Colaço, P.A. Carvalho, R. Vilar, Determination of dislocation density from hardness measurements in metals, *Mater. Lett.* 62 (2008) 3812–3814. <https://doi.org/10.1016/j.matlet.2008.04.072>.
- [10] C.P. Frick, T.W. Lang, K. Spark, K. Gall, Stress-induced martensitic transformations and shape memory at nanometer scales, *Acta Mater.* 54 (2006) 2223–2234. <https://doi.org/10.1016/j.actamat.2006.01.030>.
- [11] S. Sujith Kumar, I. Sen, A Comparative Study on Deformation Behaviour of Superelastic NiTi with Traditional Elastic–Plastic Alloys in Sub-micron Scale, *Trans. Indian Inst. Met.* (2021). <https://doi.org/10.1007/s12666-021-02207-8>.
- [12] K. Jacob, D. Yadav, S. Dixit, A. Hohenwarter, B.N. Jaya, High pressure torsion processing of maraging steel 250: Microstructure and mechanical behaviour evolution, *Mater. Sci. Eng. A.* 802 (2021) 140665. <https://doi.org/10.1016/j.msea.2020.140665>.
- [13] W.C. Oliver, G.M. Pharr, Measurement of hardness and elastic modulus by instrumented indentation: Advances in understanding and refinements to methodology, *J. Mater. Res.* 19 (2004) 3–20. <https://doi.org/10.1557/jmr.2004.19.1.3>.
- [14] S. Pathak, D. Stojakovic, S.R. Kalidindi, Measurement of the local mechanical properties in polycrystalline samples using spherical nanoindentation and orientation imaging microscopy, *Acta Mater.* 57 (2009) 3020–3028. <https://doi.org/10.1016/j.actamat.2009.03.008>.
- [15] S. Pathak, J. Shaffer, S.R. Kalidindi, Determination of an effective zero-point and extraction of indentation stress-strain curves without the continuous stiffness measurement signal, *Scr. Mater.* 60 (2009) 439–442.

<https://doi.org/10.1016/j.scriptamat.2008.11.028>.

[16] S.R. Kalidindi, S. Pathak, Determination of the effective zero-point and the extraction of spherical nanoindentation stress-strain curves, *Acta Mater.* 56 (2008) 3523–3532. <https://doi.org/10.1016/j.actamat.2008.03.036>.

[17] N.G. Mathews, A.K. Saxena, C. Kirchlechner, G. Dehm, B.N. Jaya, Effect of size and domain orientation on strength of Barium Titanate, *Scr. Mater.* 182 (2020) 68–73. <https://doi.org/10.1016/j.scriptamat.2020.02.039>.

[18] G. Dehm, B.N. Jaya, R. Raghavan, C. Kirchlechner, Overview on micro- and nanomechanical testing: New insights in interface plasticity and fracture at small length scales, *Acta Mater.* 142 (2018) 248–282. <https://doi.org/10.1016/j.actamat.2017.06.019>.

[19] J.S. Field, M. V. Swain, A simple predictivity model for spherical indentation, *J. Mater. Res.* 8 (1993) 297–306. <https://doi.org/10.1557/JMR.1993.0297>.

[20] S.K. Kang, Y.C. Kim, Y.H. Lee, J.Y. Kim, D. Kwon, Hertz elastic contact in spherical nanoindentation considering infinitesimal deformation of indenter, *Tech. Proc. 2012 NSTI Nanotechnol. Conf. Expo, NSTI-Nanotech 2012.* 1 (2012) 132–135.

[21] B.C. Maji, M. Krishnan, The effect of microstructure on the shape recovery of a Fe-Mn-Si-Cr-Ni stainless steel shape memory alloy, *Scr. Mater.* 48 (2003) 71–77. [https://doi.org/10.1016/S1359-6462\(02\)00348-2](https://doi.org/10.1016/S1359-6462(02)00348-2).

[22] X. Li, B. Bhushan, A review of nanoindentation continuous stiffness measurement technique and its applications, *Mater. Charact.* 48 (2002) 11–36. [https://doi.org/10.1016/S1044-5803\(02\)00192-4](https://doi.org/10.1016/S1044-5803(02)00192-4).